2024 IEEE International Conference on Robotics and Automation (ICRA 2024)
May 13-17, 2024. Yokohama, Japan

Vascular Centerline-Guided Autonomous Navigation Methods for Robot-Lead Endovascular Interventions

Naner Li, Yiwei Wang, *Member, IEEE*, Haoyuan Cheng,
Huan Zhao, *Member, IEEE*, and Han Ding, *Senior Member, IEEE*

***Abstract*— In minimally invasive endovascular interventional surgery, guidewire navigation is an indispensable process. However, even experienced physicians often encounter difficulties in manually manipulating the guidewire for branch selection, while also facing the risk of radiation exposure. In this study, we investigated robotic autonomous guidewire navigation methods. An electromagnetic system was used to track the real-time position and orientation of the guidewire tip, and a state space representing the guidewire within the vascular environment was constructed to guide the robot in precise guidewire manipulation. Experimental results demonstrated that the proposed trial-and-error and centerline-guided methods successfully completed navigation tasks in a static environment, outperforming human navigation performance in terms of trajectory smoothness, trajectory length, and incorrect branch entry counts. For dynamic environment navigation, dynamic time warping (DTW), a technique for measuring the similarity between two temporal sequences, was integrated into the centerline-guided method. The proposed approaches eliminate the need for visual feedback and thereby minimizing the risk of radiation exposure for both patients and medical staff present in the operating room during the procedure.**

I. INTRODUCTION

Endovascular intervention, a minimally invasive surgical procedure, offers a lower-risk alternative to traditional open surgery that treats abnormalities within blood vessels and organs by accessing them through small incisions while being guided by digital subtraction angiography (DSA) imaging. However, it leads to some occupational health concerns for physicians, such as radiation exposure [1] and orthopedic injuries [2]. To address these concerns and improve surgery outcomes, researchers have been focusing on the development of leader-follower endovascular interventional robots over the past decades [3], [4], [5].

Due to the close correlation between the shape of flexible guidewires during navigation and the vascular environment, the relationship between the movements of the guidewire's proximal and distal ends is nonlinear and varies on a case-by-case basis. It is extremely challenging to achieve precise modeling and, consequently, precise control. As a result,

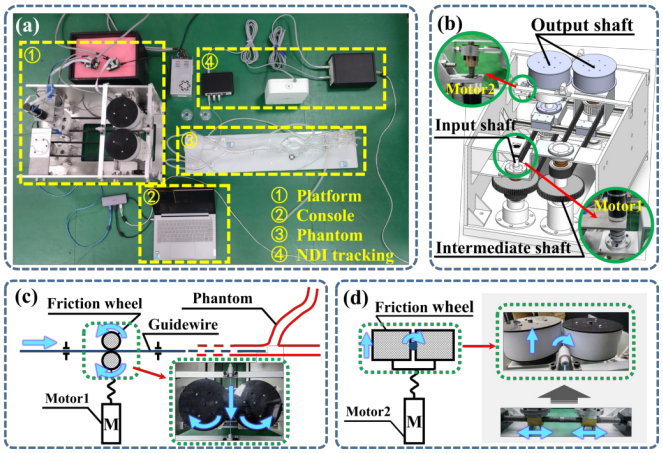

Fig. 1. (a) Illustration of the experimental setup. (b) CAD model of the designed platform. (c), (d) The working principles of the platform.

the current level of automation in vascular intervention robots remains low, requiring physicians to continue acting as decision-makers and operators. Although the utilization of finite state machines (FSM) for guidewire autonomous navigation was introduced as early as 2008 by Jayender et al. [6], research in this field has remained scarce and has not witnessed any notable advancement in the subsequent decade. Cho et al., in their 2021 study [7], employed a methodology that did not yield remarkable advancements beyond the foundational work of Jayender et al. Furthermore, both studies simplified the vascular models by flattening them into two-dimensional figures for ease of guidewire status acquisition using visual methods. This simplification also meant that the vascular models used did not fully capture the vessel thickness variations that can be encountered in real-world scenarios.

Recent advancements in artificial intelligence and machine learning algorithms have catalyzed a new wave of research into automated guidewire navigation. One approach is imitation learning, which allows intelligent agents to acquire the ability to perform tasks or make decisions in a manner similar to the expert, without explicitly understanding the underlying principles or reasoning. Zhao et al. [8] and Chi et al. [9] respectively developed a convolutional neural network and a generative adversarial network to achieve autonomous guidewire navigation, where a large amount of demonstration work was conducted by humans in the initial stage. Another approach is reinforcement learning, which enables intelligent agents to explore and optimize policies based on feedback. The researchers of Fraunhofer IPA [10] and Kweon et al. [11] respectively validated the feasibility of reinforcement learning approaches based on deep deterministic policy gradient

This work was supported in part by the National Key Research and Development Program of China under Grant 2022YFC2407402, in part by the National Science Foundation of China under Grant 62203180, in part by the Hubei Science and Technology Major Program under Grant 2023BCA002 and 2023BAA016, and in part by the Wuhan Science and Technology Major Special Project under Grant 2021022002023426.(Corresponding author: Yiwei Wang)*

The authors are with the State Key Laboratory of Intelligent Manufacturing Equipment and Technology, Huazhong University of Science and Technology, Wuhan 430074, China naner_li@hust.edu.cn; wang_yiwei@hust.edu.cn; m202170692@hust.edu.cn; huanzhao@hust.edu.cn; dinghan@mail.hust.edu.cn

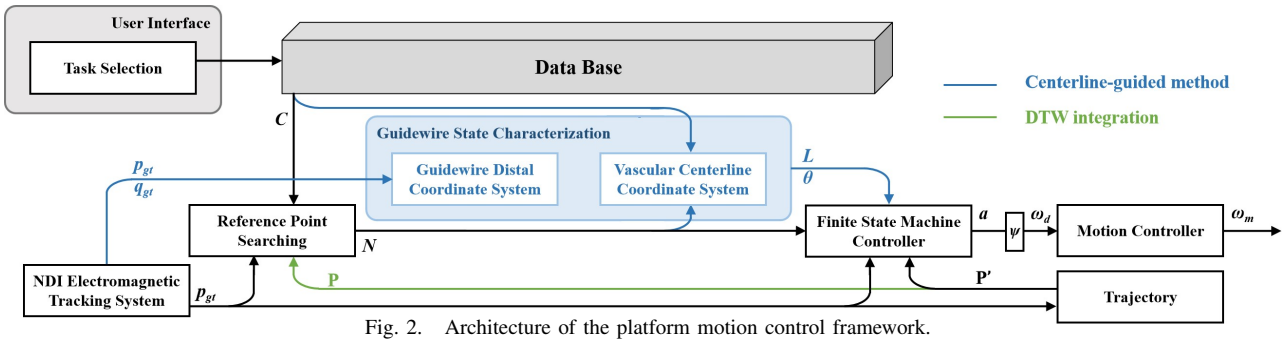

Fig. 2. Architecture of the platform motion control framework.

(DDPG) and deep Q-network (DQN). However, machine learning methods are confined by the scenarios presented during demonstrations or training. As such, their feasibility remains uncertain regarding translation to real-world settings or other vascular anatomies [12].

In actual scenarios, the vascular system is influenced by factors such as respiration, resulting in displacements and deformations of blood vessels. However, all aforementioned methods were developed based on static phantoms, and it is difficult to directly extend them for use in dynamic environments. In this study, we first propose two autonomous guidewire navigation methods based on the centerlines of blood vessels in static phantoms. Then, we introduce DTW to modify one proposed method for dynamic navigation.

II. Guidewire Manipulation Platform Design and Construction

The platform designed for guidewire manipulation essentially realizes the 2 DoFs motion by a pair of friction wheels, as shown in Fig. 1(b). Specifically, a DC motor (RE40, GP42C, Maxon Motor Inc., Switzerland) is employed to drive the input shaft while the intermediate shaft and the belts convey the movement to the output shafts, resulting in the opposite rotation of two friction wheels. As illustrated in Fig. 1(c), the guidewire thus could be pushed out and pulled back. Another DC motor (RE35, Maxon Motor Inc., Switzerland) with a screw drive (GP32S, Maxon Motor Inc., Switzerland) is applied to achieve the axial translational motion of the friction wheel, meanwhile, the guidewire is rubbed and rotated as Fig. 1(d) illustrated. The output shafts are mounted on a screw mechanism, enabling them to clamp and release the guidewire. To prevent slippage and protect the guidewire, a silicon rubber layer is added to the friction wheel. The 0.035-inch hydrophilic guidewire (RF GA35153M, Terumo Medical Co., Japan) is used in this study.

In order to enhance the realism of the experiment, a clinical-grade interventional training model (NJ005A2, Sichuan Hongchuang Jingwei Technology Co., China) is employed as the phantom, veritably replicating the anatomical configuration of human blood vessels. Moreover, an electromagnetic tracking system (Aurora, Northern Digital Inc., Canada) is applied to measure the position and orientation of the guidewire tip.

III. Autonomous Navigation Methods

Figure 2 presents the architectural layout of our platform's motion control framework, where each block represents

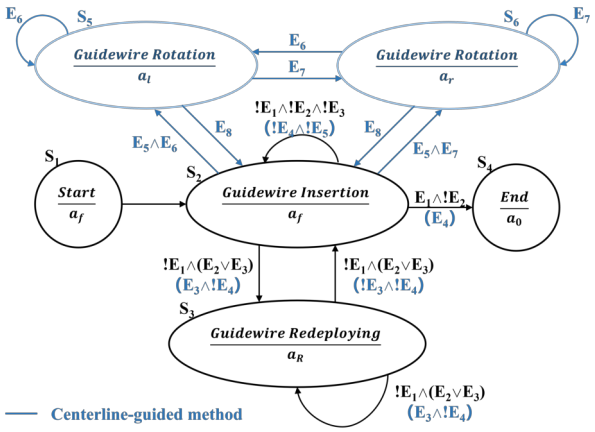

Fig. 3. Diagram for FSM: trial-and-error and centerline-guided autonomous guidewire navigation controller.

nodes implemented in ROS. The *Data Base* block serves as a repository for information about the vascular centerline. Extensive research has been conducted on various techniques for reconstructing the three-dimensional model of vasculature and extracting the vascular centerline [13], [14]. Moreover, previous studies have also highlighted the utility of centerline information in the context of guidewire navigation [15], [16], [17]. In light of this, we have premised our study on the accessibility of centerline information at the preoperative stage, and the centerline information is regarded as known information and can be used directly during the guidewire navigation. For this study, we constructed the centerline database directly from the phantom's geometric structure.

Upon task selection by the user, the *Data Base* conveys the position information $C = \{p_1, p_2, \cdots, p_N\}$ of the constituent points of the centerline of the blood vessel that the navigation task passes through to the *Reference Point Searching* node. In parallel, the NDI electromagnetic tracking system transmits the real-time positional data p_{gt} of the guidewire tip to the *Reference Point Searching* node. This node then initiates a search for the point on the centerline that is nearest to the guidewire tip, designating this point as the reference point and outputting its index $I = \arg\min_{i,p_i \in C} ||p_{gt} - p_i||$.

We have designed two types of FSM controllers: trial-and-error and centerline-guided. These controllers will be introduced in detail in the following subsection. In essence, the *FSM Controller* node retrieves information from other nodes and then generates the action a to be executed by the guidewire at the next time step. The output action is

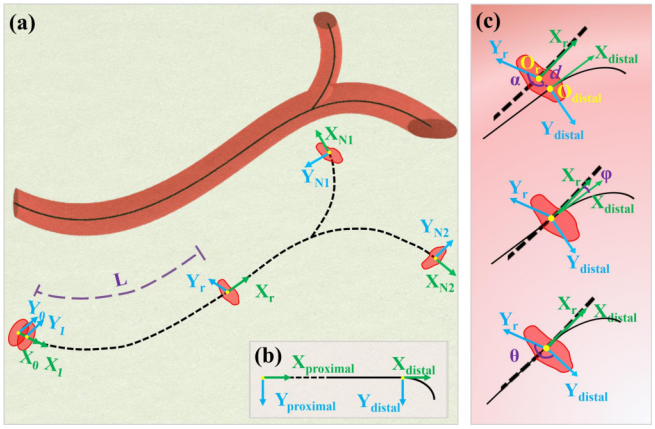

Fig. 4. Schematic of guidewire state characterization: (a) Establishing vascular centerline coordinates, (b) Defining guidewire proximal/distal coordinates, (c) Illustrating relationship between centerline and guidewire distal coordinates.

then transformed into demand values of angular velocity $\omega_d = [\omega_{d1}, \omega_{d2}]$ for the two motors of the platform through a discrete-to-continuous interface ψ. The motion controller employed is Maxon's EPOS4 controller, which incorporates a built-in velocity control loop based on a standard PI controller with feedforward. It adjusts the actual running speeds $\omega_m = [\omega_{m1}, \omega_{m2}]$ of Maxon motors according to ω_d.

A. Trial-and-Error Navigation

In clinical practice, physicians often need to make repeated attempts to enter the chosen branch when manipulating the guidewire. Therefore, inspired by the operational mode of physicians, the robot was not demanded to accomplish the branch selection at once. A proposition was put forward regarding a trial-and-error navigation approach that was formulated by a Moore-based FSM, as illustrated in Fig. 3. Mathematically, the FSM defined in this paper is described by a tuple (S, s_0, Σ, Δ, λ, δ). S denotes the state set $\{S_1, S_2, S_3, S_4\}$. s_0 denotes the initial state S_1. Σ denotes the input set $\{p_{gt}\}$. Δ represents the output set $\{a_f, a_b, a_r, a_l, a_R, a_0\}$, where the subscripts f, b, r, l, R, and 0 are utilized to represent specific movements of the guidewire. Specifically, the subscripts respectively signify movements in the forward direction, backward direction, clockwise rotation, counterclockwise rotation, a combination of actions involving retraction and simultaneous rotation by a specific angle, and the cessation of motion. $\lambda : S \times \Sigma \to \Delta$ denotes the output function. $\delta : S \times \Sigma \to S$ denotes the state transition function.

Due to the constraints imposed by the vessel wall, when the guidewire deviates from the centerline by a distance greater than a certain value, it can be considered that the guidewire has entered the wrong branch. The guidewire often encounters the common issue of becoming stuck. However, we didn't incorporate any force sensor in this study to detect such occurrences. Therefore, to prevent this situation, we define the guidewire as being stuck when the platform executes the action of pushing the guidewire forward, yet the position of the guidewire tip remains unchanged for over 3 seconds. Hence, we defined the state transition events target check E_1, path check E_2 and buckling check E_3:

$$E1: \quad ||p_{gt}(k) - p_N|| \leqslant l_L$$
$$E2: \quad ||p_{gt}(k) - p_I|| \geqslant 2 \cdot r_v$$
$$E3: \quad \Big(\sum_{k=k-3\cdot f}^{k} ||p_{gt}(k) - p_{gt}(k-1)|| \leqslant l_p\Big) \ \wedge \ (\omega_{m1} > 0)$$

where r_v represents the radius of the cross-section of the blood vessel where the guidewire tip is located, f is the sampling frequency of the trajectory points, l_L and l_P are two constants that can be manually set.

B. Centerline-Guided Navigation

Control systems usually require modeling both the tool and the environment that the tool interacts with. However, accurately describing the interaction process between the flexible guidewire and the intricate blood vessel is exceedingly challenging. In the trial-and-error navigation method, the determination of whether the guidewire is positioned within the correct branch and has reached the desired endpoint is solely based on the distances between the tip of the guidewire and the reference/endpoint. This approach lacks subjective control over the guidewire. To address this limitation, we propose a guidewire state characterization method based on the centerline of the blood vessel, which comprehensively defines the state of the guidewire within the vessel, as shown in Fig. 4.

The reference point is defined as the origin of the vascular centerline coordinate system O_r, with the tangential direction of the centerline at the reference point serving as the $\overrightarrow{X}_r$ and the normal direction serving as the $\overrightarrow{Y}_r$. The origin of the guidewire distal coordinate system O_{distal} is defined by the guidewire position p, while the $\overrightarrow{X}_{distal}$ and $\overrightarrow{Y}_{distal}$ are the guidewire axial direction and guidewire tip pre-bend direction respectively, both calculated by the unit quaternion $q_{gt} \in \mathbb{H}$ that measured by NDI system. Based on this, we can define the guidewire by [L, d, α, φ, θ]:

$$\begin{cases} L(k) = \sum_{i=1}^{N} ||p_i - p_{i-1}|| \\ d(k) = ||p_{gt}(k) - p_I|| \\ \alpha(k) = arccos\left(\dfrac{\overrightarrow{X}_r \cdot \overrightarrow{O_r O}_{distal}}{|\overrightarrow{X}_r||\overrightarrow{O_r O}_{distal}|}\right) \\ \varphi(k) = arccos\left(\dfrac{\overrightarrow{X}_r \cdot \overrightarrow{X}_{distal}}{|\overrightarrow{X}_r||\overrightarrow{X}_{distal}|}\right) \\ \theta(k) = arccos\left(\dfrac{\overrightarrow{Y}_r \cdot \overrightarrow{Y}_{distal} R_{\overrightarrow{X}_r \times \overrightarrow{X}_{distal}}(\varphi(k))}{|\overrightarrow{Y}_r||\overrightarrow{Y}_{distal} R_{\overrightarrow{X}_r \times \overrightarrow{X}_{distal}}(\varphi(k))|}\right) \end{cases} \quad (1)$$

Among these, [d, α, φ] are primarily influenced by vascular geometry. Therefore, for control purposes, we only consider [L, θ]:

$$L(k+1) = L(k) + M_L \cdot (\omega_{m1} \cdot r_f) \cdot \Delta t \cdot cos\varphi(k) + b_\theta \quad (2)$$
$$\theta(k+1) = \theta(k) + M_\theta \cdot (\omega_{m2} \cdot h / r_g) \cdot \Delta t + b_L \quad (3)$$

where M_L and M_θ are two time-varying nonlinear factors that relate to the current configuration of the guidewire; b_θ and b_L represents the interaction between two degrees of freedom motion; r_f and r_g are the radius of the friction wheel

and the guidewire; h represents the pitch of the screw drive, which is mounted on motor 2. The state transition events are listed as follows:

$$E4: \quad |L(k)-L_F| \leqslant l_L$$

$$E5: \quad |L(k)-L_b| \leqslant l_b$$

$$E6: \quad ((\theta(k) \geqslant \theta_b) \wedge (|\theta(k)-\theta_b| \leqslant 2\pi - |\theta(k)-\theta_b|)) \vee ((\theta(k) < \theta_b) \wedge (|\theta(k)-\theta_b| \geqslant 2\pi - |\theta(k)-\theta_b|))$$

$$E7: \quad ((\theta(k) \geqslant \theta_b) \wedge (|\theta(k)-\theta_b| \geqslant 2\pi - |\theta(k)-\theta_b|)) \vee ((\theta(k) < \theta_b) \wedge (|\theta(k)-\theta_b| \leqslant 2\pi - |\theta(k)-\theta_b|))$$

$$E8: \quad |\theta(k)-\theta_b| \leqslant \vartheta$$

C. DTW-Integrated Centerline Guided Navigation

The dynamic environment introduces interferences that render the simple distance-based reference point localization approach inaccurate and unreliable. Although instantaneous disturbances cause inconsistency between the vascular configuration and the original configuration, the guidewire travels inside the blood vessel, and its trajectory should strongly correlate with the geometric information of the vessel. Therefore, to properly ascertain the state of the guidewire within the vascular space, one must not only consider its current position and orientation but also incorporate historical data recording its prior trajectory. In this subsection, we proposed a DTW-based method for *Reference Point Searching* in a dynamic environment.

DTW is a method for finding the optimal matching between two, typically temporal, sequences. Initially developed for applications in speech recognition, it has gradually been applied to various other domains requiring comparative analysis of sequential data, such as gesture recognition [18]. In our particular application scenario, we consider the trajectory of the guidewire as the query sequence and the centerline as the reference sequence. By comparing the x, y, z coordinates three-dimensional features of the sampled points on the two spatial curves, we can determine the corresponding position of the guidewire tip on the centerline.

The conventional formulation for calculating the cumulative cost matrix $C(X,Y)$ in DTW is:

$$C(x_i,y_j) = D(x_i,y_j) + min(C(x_{i-1},y_j), C(x_i,y_{j-1}), C(x_{i-1},y_{j-1})) \tag{4}$$

where the $D(X,Y)$ matrix represents the Euclidean distance between the trajectory of the guidewire and the centerline.

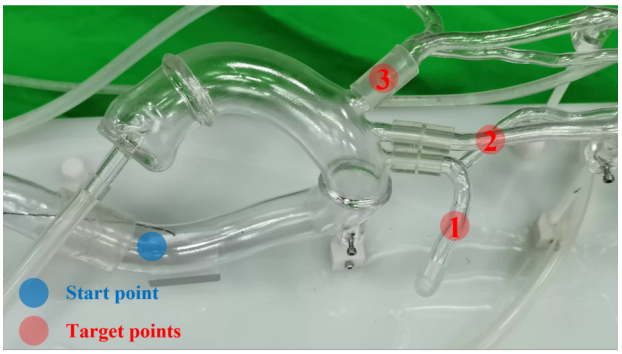

Fig. 5. Guidewire navigation tasks.

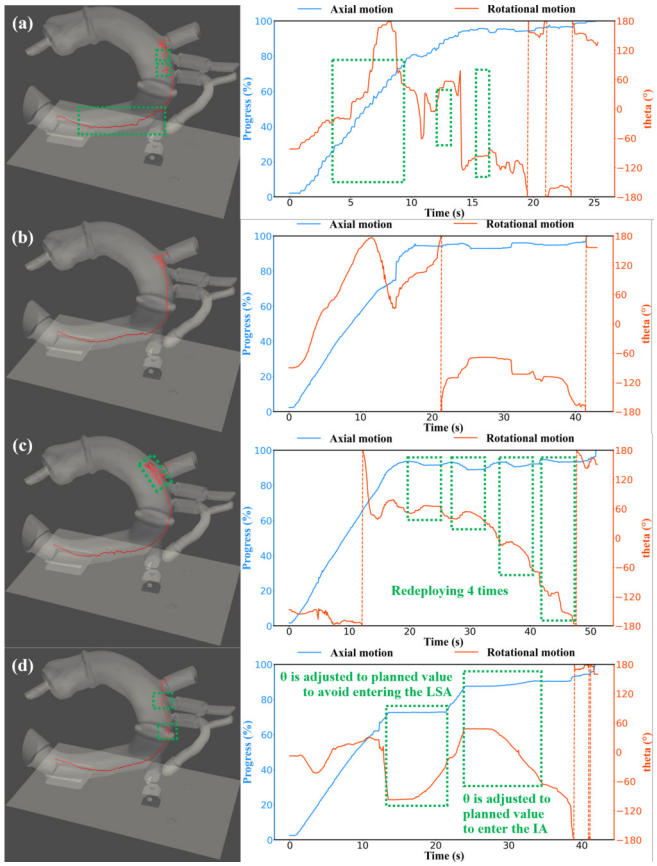

Fig. 6. Guidewire tip trajectories for Route 3 using (a) manual, (b) teleoperated, (c) trial-and-error, and (d) centerline-guided methods. The red dashed line represents continuous variation in θ values from 180° to -180° rather than a sudden change.

However, due to dynamic interferences, the trajectory will inevitably have some inconsistencies with the geometric features of the original centerline. The soft-DTW method proposed by Cuturi and Blondel [19] takes into account all possible alignments, to some extent mitigating the issue of the sole alignment that overly emphasizes these inconsistencies. The expression for soft-DTW is as follows:

$$C(x_i,y_j) = D(x_i,y_j) + min^{\gamma}(C(x_{i-1},y_j), C(x_i,y_{j-1}), C(x_{i-1},y_{j-1})) \tag{5}$$

with

$$min^{\gamma}(a_1,\cdots,a_n) = \begin{cases} min_{i\leq n} a_i, & \gamma = 0 \\ -\gamma log \sum_{i=1}^{n} e^{-a_i/\gamma}, & \gamma > 0 \end{cases} \tag{6}$$

where γ is a smoothing hyper-parameter that represents the permissible extent of alignment offset. In this context, we have empirically opted to assign a value of 0.1 to γ.

Given that the trajectory of the guidewire is a sequence that is still being generated, whereas the centerline is a complete sequence, we cannot directly align the two sequences. Therefore, we applied an open-end boundary condition (OE) that allows the alignment to end at any point at the last row of the cumulative cost matrix [20]. The alignment cost of OE-DTW is defined by the minimum value in the last row:

$$OE-DTW(X,Y) = min_{j=1,2,\cdots,m} DTW(X,Y_j) \tag{7}$$

so far, the reference point index I has been founded and defined by j.

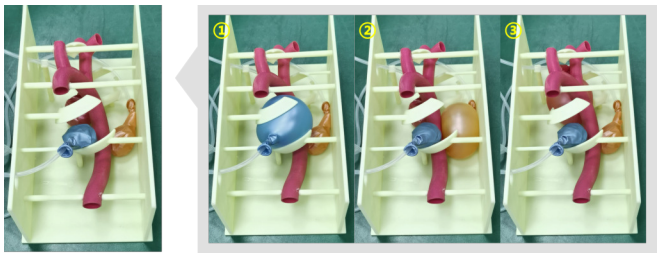

Fig. 7. Dynamic experimental environment comprising soft phantom and inflated balloons.

To minimize computational costs and maximize processing efficiency, we have omitted the trace-back process. Additionally, a GPU-based parallelization technique [21] has been implemented to further accelerate the computation.

IV. Experiments and Results

A. Experiment in Static Phantom

1) Task Specification: The experimental scene we designed involves guidewire navigation starting from the descending aorta and terminating at three distinct target locations. As depicted in Fig. 5, route 1 requires the guidewire to enter the narrow left subclavian artery (LSA) from the spacious region of the aortic arch while avoiding the branching vessel to reach target 1. Similarly, route 2 requires initial access to LSA but demands further maneuvering towards target 2 by selecting an even narrower pathway through the left vertebral artery (LVA) at its bifurcation point. Route 3 needs the guidewire bypassing both LSA and left common carotid artery (LCCA), before gaining access to the innominate artery (IA). This design aims to encompass a comprehensive range of scenarios including blood vessel thickness variation and configuration differences for the validation of the proposed autonomous navigation methods.

2) Results: In our study, we employed four distinct methods to perform navigation tasks along three routes: the manual operation method, teleoperation method via the console, trial-and-error method, and centerline-guided method. Each method was repeated eight times for each route, resulting in a total of 96 experiments. Both of the proposed autonomous navigation methods demonstrated successful completion of the navigation tasks.

To quantitatively analyze the performance of the four different methods, we consolidated and presented the experimental results in Table I. Overall, the manual operation method exhibited the highest speed and shortest duration. This can primarily be attributed to the other methods being constrained by the speed of the robotic platform. However, the standard deviation of the speed (STDEV speed) for the methods executed by the platform was relatively low. A lower STDEV speed implies less variation in the speed of the guidewire tip, indicating a more stable guidewire navigation process and a reduced risk of vessel damage and embolization.

Although the platform speed remained constant, both the teleoperation and centerline-guided methods exhibited lower speeds compared to the trial-and-error method. This discrepancy can be attributed to the idle time required for cognitive processing during human-teleoperated tasks and the fact that the actual speed of the guidewire tip approaches zero when the centerline-guided method adjusts θ. While the centerline-guided method demonstrated a relatively low mean speed, it excelled in avoiding erroneous branches and successfully navigating towards the planned path. Consequently, it exhibited the shortest execution trajectory among all the methods and the shortest execution time among the methods conducted by the robotic platform.

When considering the different routes, route 3 presented greater difficulty in completion compared to routes 1 and 2. This resulted in an overall longer time consumption and a higher likelihood of the guidewire entering incorrect branches. The wider IA compared to LSA made it challenging for the guidewire to receive sufficient support from the vessel wall. However, the proposed centerline-guided method maintained its performance in achieving precise insertion.

Figure 6 depicts examples of the guidewire tip trajectories. It is evident from the figure that the trajectory of the guidewire tip appears jagged when operated by a human compared to the robotic platform. Even slight unintentional movements in the rotational direction can cause drastic changes in the orientation of the guidewire tip. This observation aligns with the results indicated by STDEV speed.

It is important to note that the phantom used in the experiments was transparent, allowing direct observation of the guidewire's state during operation. This significantly simplified the task difficulty for the manual and teleoperated methods. If actual DSA imaging was employed for visual feedback, we anticipate that operators would likely be less sensitive, resulting in a higher count of wrong branch entries, longer trajectories, and increased task execution time.

TABLE I

Mean value ± std of performance metrics for manual, teleoperated and autonomous endovascular intervention.

		Mean Speed (mm/s)	STDEV Speed (mm/s)	Trajectory Length (mm)	Procedure Duration (s)	Wrong Branch Entry Counts
Route 1	Manual	**15.311 ±1.728**	**18.996 ±2.527**	**364.274 ±17.068**	**24.048 ±2.891**	0.250 ± 0.463
	Teleoperated	**7.059 ±1.091**	10.921 ± 1.529	**350.307 ±59.376**	**51.639 ±16.949**	0.500 ± 0.756
	Trial-and-Error	9.745 ± 3.135	15.326 ± 1.820	**481.657 ±180.824**	56.372 ± 33.295	**2.750 ±2.493**
	Centerline-Guided	8.749 ± 0.716	13.292 ± 3.613	282.935 ± 27.788	32.353 ± 1.869	0.000 ± 0.000
Route 2	Manual	**13.516 ±1.253**	**17.426 ±2.079**	**393.287 ±85.625**	29.423 ± 7.892	0.375 ± 0.744
	Teleoperated	**6.763 ±0.501**	11.105 ± 1.562	**327.923 ±66.889**	**48.840 ±11.524**	**0.500 ±0.535**
	Trial-and-Error	**10.535 ±1.101**	**15.750 ±2.061**	**357.792 ±46.299**	34.566 ± 7.574	**1.500 ±0.756**
	Centerline-Guided	7.675 ± 0.813	10.484 ± 1.334	273.508 ± 8.506	35.981 ± 3.856	0.000 ± 0.000
Route 3	Manual	**14.230 ±3.323**	**20.149 ±4.609**	**359.594 ±55.888**	**26.628 ±7.518**	0.750 ± 1.035
	Teleoperated	6.569 ± 1.129	**11.741 ±1.457**	**417.431 ±82.727**	**66.910 ±24.105**	**1.500 ±0.926**
	Trial-and-Error	**8.848 ±0.695**	**11.708 ±1.158**	**671.019 ±215.512**	**77.694 ±30.186**	**6.571 ±3.552**
	Centerline-Guided	6.688 ± 0.591	9.433 ± 1.076	287.823 ± 15.701	43.152 ± 1.927	0.000 ± 0.000

Bold represents statistically significant results comparing to the centerline-guided approach ($p < 0.05$)

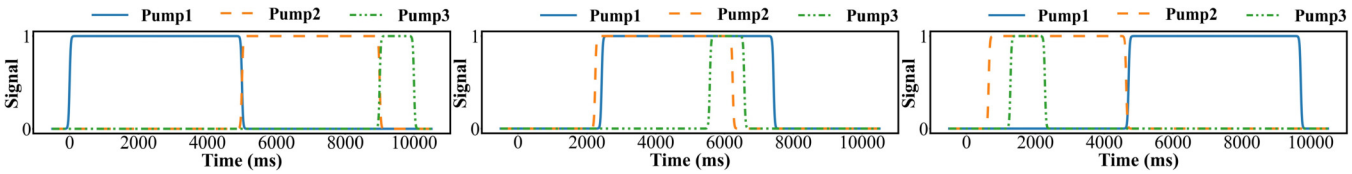

Fig. 8. Inflating patterns for balloons.

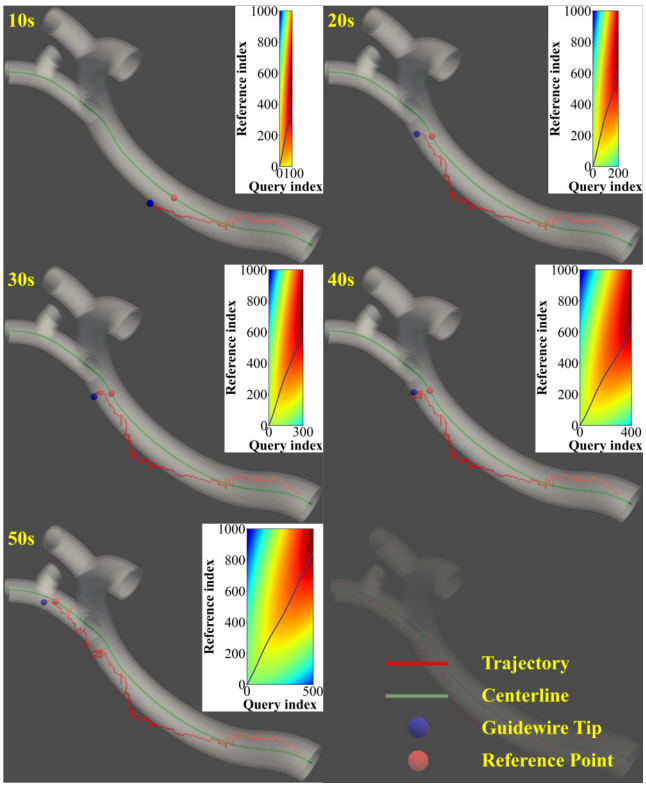

Fig. 9. An illustrative example of guidewire tip trajectories following route 2 with balloon inflating pattern 1.

B. Experiment in Dynamic Phantom

1) Task Specification: Owing to the impact of respiration and body movements, the blood vessels undergo changes in position and morphology. While external markers can effectively mitigate overall postural changes, the internal tissue displacement resulting from respiration poses challenges in terms of measurement and modeling. To introduce this dynamic interference, we utilized 3D printing technology to construct a soft vascular model and placed three balloons at different positions. The expansion and contraction of these balloons generated the desired dynamic interference, as shown in Fig. 7. In addition to multiple interference sources, we also employed various patterns of interference to verify the proposed method's feasibility under random disturbances. As shown in Fig. 8, we established three different patterns for inflating the balloons. One pattern involved sequentially inflating the three balloons within one cycle, while the other two patterns involved random numbers to determine the starting time for inflating each balloon within one cycle. It was crucial to set the inflation times for the three balloons. If inflation time was insufficient, the blood vessels would not be effectively disturbed; if the inflation time was too long, the balloons might explode due to the constraints of external supports. Therefore, we manually set the inflation times for the three balloons based on their placements: 5000 ms, 4000 ms, and 1000 ms. These durations were selected to ensure a maximum displacement of approximately 15 mm, surpassing the tissue displacement caused by actual respiratory motion at the millimeter scale [22]. Lastly, the navigation routes remained the same.

2) Results: Figure 9 demonstrates an example of the guidewire tip trajectories aiming at target 2 with balloon inflating pattern 1. The red line represents the trajectory of the guidewire, the green line represents the centerline, the blue sphere represents the current position of the guidewire tip, and the red sphere represents the corresponding point on the centerline computed by OE-soft-DTW. From the figure, it can be observed that the red trajectory is affected by external disturbances, resulting in deviations from the original configuration of the blood vessel.

This experiment serves as a proof-of-concept for the proposed method. The experimental results indicate that the proposed method can successfully accomplish the navigation task under various navigation routes and interference conditions. This verifies the potential and feasibility of the proposed method for autonomous guidewire navigation under dynamic influences.

V. Conclusion

The proposed autonomous guidewire navigation methods have been empirically validated as effective in static and dynamic environments. The centerline-guided method has demonstrated outstanding performance across critical metrics, including relatively low STDEV speed, short trajectory length, brief procedure duration, and minimal wrong branch entries. This exceptional performance directly correlates with a reduced likelihood of procedural complications, thereby enhancing patient safety and overall outcomes. Furthermore, the utilization of preoperatively acquired centerline information eliminates the need for intraoperative DSA imaging. Consequently, not only is the risk of radiation exposure to physicians mitigated, but patients and other medical personnel in the operating room are also shielded from radiation exposure.

Although we attempted to simulate real dynamic environments as much as possible by employing multiple navigation routes and various interference patterns, the covered scenarios are still limited, and the proposed method may fail in complex rare situations (e.g., blood vessel penetration) that are not encompassed within this study. Additionally, due to the unreliability of distance information in dynamic environments, the proposed DTW-integrated centerline-guided navigation method cannot determine if the guidewire has entered an incorrect branch. Further research endeavors can aim to address these limitations.

REFERENCES

[1] M. G. Andreassi, E. Piccaluga, L. Gargani, L. Sabatino, A. Borghini, F. Faita, R. M. Bruno, R. Padovani, G. Guagliumi, and E. Picano, "Subclinical carotid atherosclerosis and early vascular aging from long-term low-dose ionizing radiation exposure: a genetic, telomere, and vascular ultrasound study in cardiac catheterization laboratory staff," *JACC: Cardiovascular Interventions*, vol. 8, no. 4, pp. 616–627, 2015.

[2] M. G. Andreassi, E. Piccaluga, G. Guagliumi, M. Del Greco, F. Gaita, and E. Picano, "Occupational health risks in cardiac catheterization laboratory workers," *Circulation: Cardiovascular Interventions*, vol. 9, no. 4, p. e003273, 2016.

[3] H. Rafii-Tari, C. V. Riga, C. J. Payne, M. S. Hamady, N. J. Cheshire, C. D. Bicknell, and G.-Z. Yang, "Reducing contact forces in the arch and supra-aortic vessels using the magellan robot," *Journal of Vascular Surgery*, vol. 64, no. 5, pp. 1422–1432, 2016.

[4] C. C. Smitson, L. Ang, A. Pourdjabbar, R. Reeves, M. Patel, and E. Mahmud, "Safety and feasibility of a novel, second-generation robotic-assisted system for percutaneous coronary intervention: first-in-human report," *Journal of invasive cardiology*, vol. 30, no. 4, pp. 152–156, 2018.

[5] E. M. Khan, W. Frumkin, G. A. Ng, S. Neelagaru, F. M. Abi-Samra, J. Lee, M. Giudici, D. Gohn, R. A. Winkle, J. Sussman *et al.*, "First experience with a novel robotic remote catheter system: Amigo™ mapping trial," *Journal of Interventional Cardiac Electrophysiology*, vol. 37, no. 2, pp. 121–129, 2013.

[6] J. Jayender, M. Azizian, and R. V. Patel, "Autonomous image-guided robot-assisted active catheter insertion," *IEEE Transactions on Robotics*, vol. 24, no. 4, pp. 858–871, 2008.

[7] Y. Cho, J.-H. Park, J. Choi, and D. E. Chang, "Image processing based autonomous guidewire navigation in percutaneous coronary intervention," in *2021 IEEE International Conference on Consumer Electronics-Asia (ICCE-Asia)*. IEEE, 2021, pp. 1–6.

[8] Y. Zhao, S. Guo, Y. Wang, J. Cui, Y. Ma, Y. Zeng, X. Liu, Y. Jiang, Y. Li, L. Shi *et al.*, "A cnn-based prototype method of unstructured surgical state perception and navigation for an endovascular surgery robot," *Medical & Biological Engineering & Computing*, vol. 57, no. 9, pp. 1875–1887, 2019.

[9] W. Chi, G. Dagnino, T. M. Kwok, A. Nguyen, D. Kundrat, M. E. Abdelaziz, C. Riga, C. Bicknell, and G.-Z. Yang, "Collaborative robot-assisted endovascular catheterization with generative adversarial imitation learning," in *2020 IEEE International Conference on Robotics and Automation (ICRA)*. IEEE, 2020, pp. 2414–2420.

[10] L. Karstensen, T. Behr, T. P. Pusch, F. Mathis-Ullrich, and J. Stallkamp, "Autonomous guidewire navigation in a two dimensional vascular phantom," *Current Directions in Biomedical Engineering*, vol. 6, no. 1, p. 20200007, 2020.

[11] J. Kweon, K. Kim, C. Lee, H. Kwon, J. Park, K. Song, Y. I. Kim, J. Park, I. Back, J.-H. Roh *et al.*, "Deep reinforcement learning for guidewire navigation in coronary artery phantom," *IEEE Access*, vol. 9, pp. 166 409–166 422, 2021.

[12] L. Karstensen, J. Ritter, J. Hatzl, T. Pätz, J. Langejürgen, C. Uhl, and F. Mathis-Ullrich, "Learning-based autonomous vascular guidewire navigation without human demonstration in the venous system of a porcine liver," *International Journal of Computer Assisted Radiology and Surgery*, vol. 17, pp. 2033–2040, 2022.

[13] X. Sheng, T. Fan, X. Jin, J. Jin, Z. Chen, G. Zheng, M. Lu, and Z. Zhu, "Extraction method of coronary artery blood vessel centerline in ct coronary angiography," *IEEE Access*, vol. 7, pp. 170 690–170 702, 2019.

[14] Y. Zhang, R. Falque, L. Zhao, Y. Chen, S. Huang, and H. Li, "Structure-to-shape aortic 3-d deformation reconstruction for endovascular interventions," *IEEE Transactions on Robotics*, pp. 2954–2972, 2023.

[15] C. Ji, Z. G. Hou, and X. L. Xie, "An image-based guidewire navigation method for robot-assisted intravascular interventions," in *International Conference of the IEEE Engineering in Medicine Biology Society*, 2011, pp. 6680–6685.

[16] F. Langsch, S. Virga, J. Esteban, R. Göbl, and N. Navab, "Robotic ultrasound for catheter navigation in endovascular procedures," in *2019 IEEE/RSJ International Conference on Intelligent Robots and Systems (IROS)*. IEEE, 2019, pp. 5404–5410.

[17] W. Chi, J. Liu, M. E. Abdelaziz, G. Dagnino, C. Riga, C. Bicknell, and G.-Z. Yang, "Trajectory optimization of robot-assisted endovascular catheterization with reinforcement learning," in *2018 IEEE/RSJ International Conference on Intelligent Robots and Systems (IROS)*. IEEE, 2018, pp. 3875–3881.

[18] H. Walugembe, C. Phillips, J. Requena-Carrion, and T. Timotijevic, "Comparing dynamic hand rehabilitation gestures in leap motion using multi-dimensional dynamic time warping," *IEEE Sensors Journal*, vol. 21, no. 6, pp. 8002–8010, 2020.

[19] M. Cuturi and M. Blondel, "Soft-dtw: a differentiable loss function for time-series," in *International conference on machine learning*. PMLR, 2017, pp. 894–903.

[20] P. Tormene, T. Giorgino, S. Quaglini, and M. Stefanelli, "Matching incomplete time series with dynamic time warping: an algorithm and an application to post-stroke rehabilitation," *Artificial intelligence in medicine*, vol. 45, no. 1, pp. 11–34, 2009.

[21] H. Zhu, Z. Gu, H. Zhao, K. Chen, C.-T. Li, and L. He, "Developing a pattern discovery method in time series data and its gpu acceleration," *Big Data Mining and Analytics*, vol. 1, no. 4, pp. 266–283, 2018.

[22] A. De Groote, M. Wantier, G. Chéron, M. Estenne, and M. Paiva, "Chest wall motion during tidal breathing," *Journal of Applied Physiology*, vol. 83, no. 5, pp. 1531–1537, 1997.